MATERIALS SCIENCE

Asymmetric tacticity navigates the localized metal spin state for sustainable alkaline/sea water oxidation

Yaoda Liu[1], Lei Li[1], Xuning Li[2], Yifan Xu[3], Dongshuang Wu[3], Thangavel Sakthivel[4], Zhixin Guo[1], Xiaoxu Zhao[5], Zhengfei Dai[1]*

Anodic oxygen evolution reaction (OER) that involves a spin-dependent singlet-to-triplet oxygen changeover largely restrains the water electrolysis efficiency for hydrogen production. However, the modulation of spin state is still challengeable for most OER catalysts, and there remains a debate on deciphering the active spin state in OER. Here, we pioneered an asymmetric Fe-incorporated $NiPS_3$ tactic system to retune the metal localized spin for efficient OER electrocatalysis. It is unraveled that the synergistic effect of medium-spin Fe^{III} site and P/S coordination can effectively boost OER activity and Cl resistance selectivity in alkaline/sea water. Resultantly, the Fe/$NiPS_3$-based asymmetric electrodes exhibit low cell voltages of 1.50 volts/1.52 volts in alkaline/sea water at 10 milliamperes per square centimeter, together with a sustainable retention for 1000 hours. It also delivers the durable performance in anion exchange membrane water electrolyzers with a low operation voltage at 45°C. This research navigates the atomic localized spin state as the criterion in rationalizing efficient nonprecious alkaline/sea water oxidation electrocatalysts.

INTRODUCTION

Water electrolysis (WE) holds the fossil-free promise for green hydrogen production for future carbon-neutral society (*1*, *2*). However, the WE deployment still suffers from anodic sluggish oxygen evolution reaction (OER) and the reliance on precious catalysts (*3*). It is essential to design active and economic electrocatalysts to effectuate the kinetic enhancement for OER (*4*, *5*). In principle, the OER kinetics is restrained not only from the four-electron pathway but also from the oxygen spin state change (*6*, *7*). During the OER, it occurs the spin-correlated transfer (Fig. 1A) from the diamagnetic singlet H_2O/OH^- to the triplet state O_2 ($\uparrow O{=}O\uparrow$, paramagnetic) (*8*). Note that such a singlet → triplet associated spin state transition is normally energy barriered from the classic spin selection rule (*9*). Hence, a range of researchers has applied the magnetic field to deblock the spin suppression to kinetically drive the OER (*10*, *11*). Owing to the tunable spin state, a NiFe bimetallic system is deemed as a typical platform for localized magnetization-scaled OER studies (*12*). In particular, the Fe ion with unpaired spin electrons (Fig. 1B) at the e_g/t_{2g} orbitals can carry forward the spin-related electron exchange with oxygen intermediates in OER (*8*). However, there still remains a debate in the origin of magnetic field–enhanced OER behaviors, whether it is from microconvection, microwave heating, or magnetocaloric effect (*13*). Hence, a field-free manner is rather desired to gain a clear understanding and rational innovation of the spin-impacted OER electrocatalysis.

As the triplet O_2 ($\uparrow O{=}O\uparrow$) is involved, it may occur spin flips in the OER reactants or electrocatalysts (*14*). Set aside the magnetic effect, the engineering of atomic localized spin arrangement is the ground rule to reap the spin-correlated OER catalysis (*15*). Theoretical investigations have concluded that a catalyst with atomic ferromagnetic (FM) ordering would facilitate the spin-selective electron transfer from singlet reactants toward triplet O_2 (*10*). While most OER-active catalysts are antiferromagnetic (AFM) at room temperature (RT), it is still challenging and highly desirable to realize the atomic FM catalysts of spontaneous polarization without magnetic field (*16*). Besides, the OER electrocatalysis is rather susceptible to impurities in the electrolyte, such as the Cl^- in saline seawater (*17*, *18*). The two-electron Cl oxidation reaction (ClOR) will compete with OER in seawater (SOER), leading to the corrosion and efficiency drop to the electrolyzer (*19*). Current strategies for the SOER/ClOR selectivity are mainly on the regulation of Cl/O affinity at the catalytic sites, but the Cl^- adsorb ability is dynamically changed with the applied potential (*20*, *21*). The inhibition of ClOR still appeals for an intrinsically selective methodology. From the viewpoint of electronic spin, the ClOR process from Cl^- to Cl_2 does not involve spin state evolution (Fig. 1A). The different spin modes between OER and ClOR might navigate an innovative paradigm toward the OER selectivity, but it is rarely explored in seawater oxidation. Hence, the efficient alkaline/seawater oxidation necessitates the rational design of the FM electrocatalysts with field-free localized spin state modulations.

In this work, we pioneered an asymmetric Fe-incorporated $NiPS_3$ (Fe/$NiPS_3$) system as the electrocatalytic platform without external magnetic field for OER performance and spin-adaptive mechanistic studies. The introduction of Fe causes lattice distortion and regulates the local electronic structure on the $NiPS_3$. Detailed theoretical and experimental analyses have elucidated the hypothesis of localized spin state modulation and strong OER/ClOR selectivity in the Fe/$NiPS_3$ precatalyst and reconstructed P/S-doped NiFeOOH system. It is unraveled that the medium-spin (MS) Fe^{III} site can grant the evolution of OER intermediates more energetically. In the entire systems, the exposure of Fe active centers with P/S sacrificial sites jointly inhibits the ClOR toward the enhanced OER selectivity. As in the asymmetric WE, the Fe/$NiPS_3$||Pt/C electrode pair exhibits low cell voltages of 1.50 V in alkaline water and 1.52 V in seawater at 10 mA cm^{-2}, together with a sustainable retention for 1000 hours. It also showcases the

[1]State Key Laboratory for Mechanical Behavior of Materials, Xi'an Jiaotong University, Xi'an 710049, P. R. China. [2]State Key Laboratory of Catalysis, Dalian Institute of Chemical Physics, Chinese Academy of Sciences, Dalian 116023, P. R. China. [3]School of Materials Science and Engineering, Nanyang Technological University, Singapore 639798, Singapore. [4]Department of Chemical Engineering, Kumoh National Institute of Technology, Gyeongbuk 39177, South Korea. [5]School of Materials Science and Engineering, Peking University, Beijing 100871, P. R. China.
*Corresponding author. Email: sensdai@mail.xjtu.edu.cn

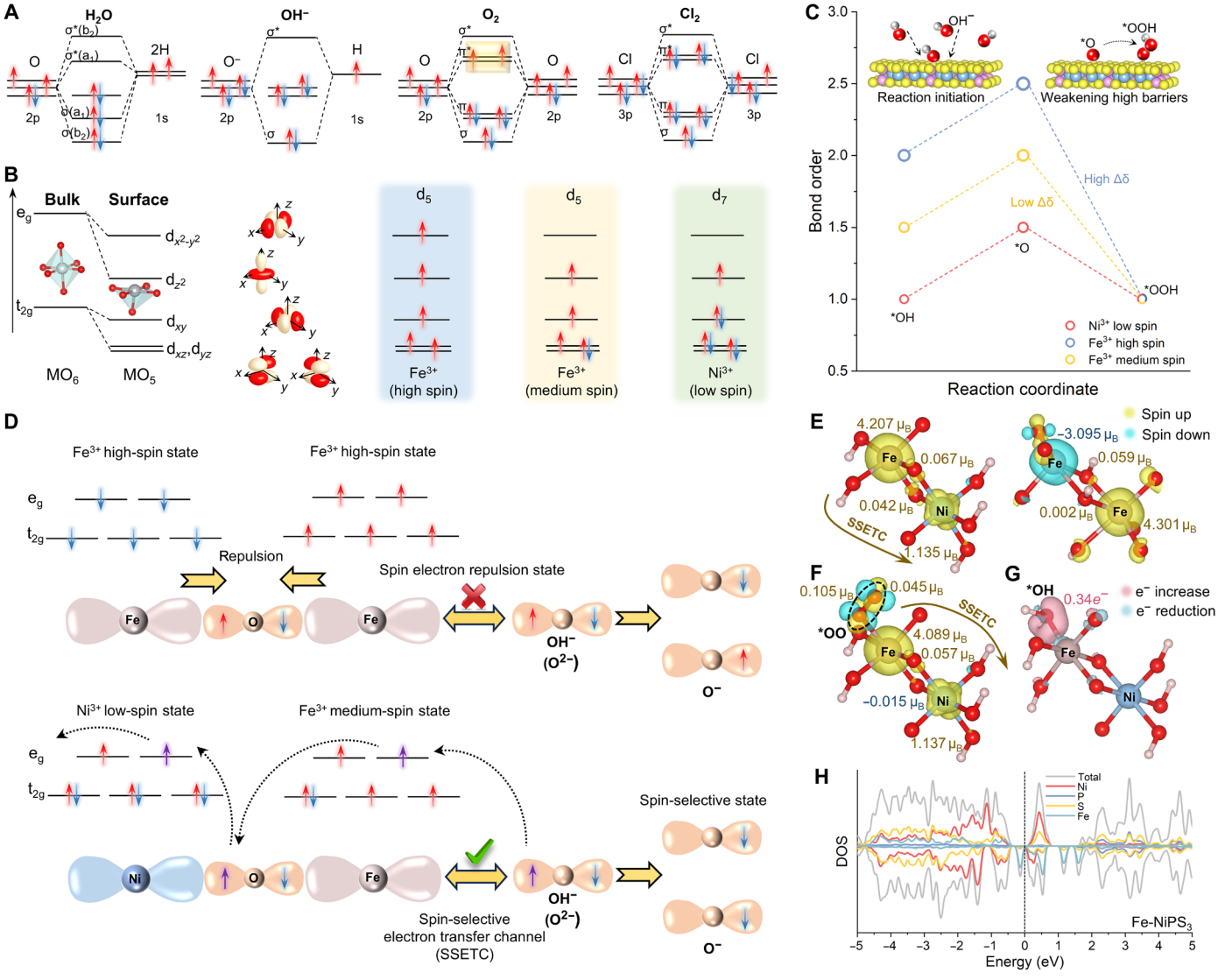

Fig. 1. Rationales of the localized spin state adaptation for alkaline/sea water oxidation electrocatalysis. (**A**) Molecular orbital diagrams of H_2O, OH^-, O_2, and Cl_2. (**B**) d-Electron configurations of iron and nickel cations with different spin states at the surface. (**C**) Bond order (δ) of OER intermediates adsorbed by various cations, here δ = (number of bonding electrons − number of antibonding electrons)/2. (**D**) Schematic illustration of the spin-selective channel in a single Fe site and NiFe dual sites, along with corresponding evolution of O-containing substances. (**E**) The spin density pattern of Fe—Ni and Fe—Fe couple in oxyhydroxides, and the isosurface level was set as 0.02 *e* Å^{-3}. (**F**) The spin density pattern of Fe—Ni couple absorbed with *OO, and the isosurface level was set as 0.02 *e* Å^{-3}. (**G**) The charge density difference between *OH and Fe—Ni couple, and the isosurface level was set as 0.01 *e* Å^{-3}. (**H**) DOS of Fe/$NiPS_3$.

power-saving and stable performance in the practical anion exchange membrane (sea)water electrolysis [AEM(S)WE] devices. This study navigates the localized spin state adaptation as a fundamental criterion for rationalizing active and selective water oxidation electrocatalysts.

RESULTS

Theoretical viewpoint for localized spin state adaptation

Since the high spin (HS)/MS and low spin are relatively stable spin configurations for Fe^{3+} and Ni^{3+} in oxyhydroxides (the active species after OER reconstruction), we thus carried out an analysis of the interaction between these cations and adsorbed OER intermediates (Fig. 1B and fig. S1). The d_{x2-y2} and d_{xy} orbitals are omitted on the basis of symmetry conservation (*8*). The bond order (δ) between different intermediates and cations was evaluated (Fig. 1C), where a larger δ value represents the higher adsorption strength (*22*). Thermodynamically, a strong *OH adsorption is the prerequisite for initiating the OER, and the *OOH adsorption strength should be weaker than that of *OH for the sustainable OER cycle. The δ values of *OH and *OOH at Ni^{3+} site are equal; whereas at HS Fe^{3+} and MS Fe^{3+} sites, the δ values of *OH are higher than that of *OOH. This suggests that Fe sites are more compatible with OER occurrence than Ni sites in terms of the localized spin state. Because the third step ($*O + OH^- \rightarrow *OOH + e^-$) is usually the rate-determining step (RDS) in OER (*23*), the MS Fe^{3+} with lower $\Delta\delta_{*O \rightarrow *OOH}$ will be more eligible to kinetically drive the OER than HS Fe^{3+} in trend.

As witnessed that NiFe bimetallic catalysts always perform well in OER over the single Fe cases (*24*), there might exist electronic interaction between Ni and Fe sites. We thus analyze the spin-correlated electron transfer mechanisms in bare Fe^{3+} and bimetallic Ni^{3+}/Fe^{3+} oxyhydroxides (usually the reconstructed active products during OER), as depicted in Fig. 1D. For the bare Fe^{3+} case, the neighboring HS Fe^{3+} sites illustrate different upward and downward spins, impeding the spin-selective electron migration in OER. In contrast, the presence of Ni^{3+} induces the generation of MS Fe^{3+} to establish a spin-selective e^- transfer channel (SSETC) in the Fe-O-Ni bridge, giving rise to the intermediates with fixed spin direction [$O^-(\downarrow)$] (*25*, *26*). These intermediates can kinetically form the triplet $O^{(\downarrow)}O^{(\downarrow)}H$* intermediate for efficient O_2 release. Moreover, the ClOR process involves two different-spin Cl species (↑Cl—Cl↓) for Cl_2 evolution (fig. S2), so the Ni/Fe coupling will be an appropriate choice for spin-boosted OER with high selectivity (*27*). Density functional theory (DFT) calculations provide a more intuitive understanding of OER enhancement mechanisms based on SSETC. Only the Fe—Ni configuration can induce the O at the junction to produce the same spin direction and form efficient SSETC in the Fe-O-Ni linkage (Fig. 1E and figs. S3 to S5). In other words, metal-O-metal atoms with the same main spin density direction can form SSETC channels and thus facilitate the transfer of electrons (fig. S5B). When *OO is adsorbed, the Fe—Ni couple and the *OO will jointly generate a SSETC manner for spin-up electrons (Fig. 1F) and induce the emergence of spin-down triplet O_2 (↓O═O↓; fig. S6A). However, the Fe—Fe or Ni—Ni couple cannot effectively conduct the selective electron transfer for the generation of triplet O_2 (fig. S6, B and C). For the adsorption of *ClCl, the dominant SSETC in the Fe—Ni couple inhibits the generation of spin-reversed ↑Cl—Cl↓ state (fig. S7). In addition, the charge density difference results show that there is more charge transfer between *OH and Fe—Ni couple (Fig. 1G) than that of Ni—Ni and Fe—Fe cases (fig. S8). It is worth noting that consistent with the bond order analysis, the Fe site exhibits more active *OH adsorption than the Ni site (fig. S9A). Besides, the Fe—Ni couple with the advantageous SSETC shows the smallest OER reaction energy barrier (fig. S5C). In addition, the coordination of P and S will further reduce and tune the spin state of Fe (fig. S9B), combining both energetic and spin-selective advantages.

On the basis of this, an electrically conductive and OER-active $NiPS_3$ structure was chosen as the platform for Fe modification (fig. S10). Relative to pure $NiPS_3$ (fig. S11, A and B), the $Fe/NiPS_3$ asymmetric tacticity endows the enhanced spin electron density (fig. S12A) and more delocalized electron distribution (fig. S12B) at the Fe site. From the density of state (DOS) result, pure $NiPS_3$ exhibits the AFM and semiconductor characteristics with a bandgap (fig. S11C). In contrast, the $Fe/NiPS_3$ features with the FM state and half-metallic DOS (Fig. 1H). Hence, the incorporation of Fe into $NiPS_3$ to trigger the asymmetric tacticity is beneficial for electron transfer and localized spin state optimization in OER catalysis. It provides a structural basis for the derivation of P/S-coordinated Fe—Ni configuration.

Microstructures, phase, and chemical states

The coupling of Fe into $NiPS_3$ was conducted by an ultrafast (10 s) aqueous process, as schemed in Fig. 2A. It starts from the high-yield electrochemical exfoliation of bulk $NiPS_3$ crystals (Fig. 2B) to few-layer $NiPS_3$ nanosheets (EE-$NiPS_3$; Fig. 2C and fig. S13) (*28*). The atomic force microscope test results indicate that the thickness of EE-$NiPS_3$ is approximately 2.70 nm (fig. S14). Afterward, the Fe/$NiPS_3$ materials were prepared with the fast mixing of hot Fe^{3+} solution with EE-$NiPS_3$. A series of Fe/$NiPS_3$ samples were synthesized by adjusting the concentration of Fe^{3+} (fig. S15), as denoted as Fe/$NiPS_3$-x (x = 1 to 6). In the subsequent descriptions, the Fe/$NiPS_3$ refers to the Fe/$NiPS_3$-4 sample prepared from moderate Fe^{3+} concentration. Compared with EE-$NiPS_3$ nanosheets, the Fe/$NiPS_3$ sample exhibits a notably granular rough surface morphology (Fig. 2D and fig. S15D). In addition, samples synthesized from other concentrations also exhibit varying degrees of surface roughness (fig. S15). As a reference, the $NiPS_3$ samples with other Co, Ni, and Mo ion modifications were also synthesized (figs. S16 to S18). The aberration-corrected bright-field scanning transmission electron microscopy (BF-STEM) image (Fig. 2E) and transmission electron microscopy (TEM) images (fig. S19) of Fe/$NiPS_3$ also illustrate that the nanosheet morphology is well maintained after the Fe^{3+}-$NiPS_3$ reaction. Combined with the high-angle annular dark field STEM images in fig. S20, it can be observed that the roughness and thickness contrast of the nanosheet surface change after Fe introduction. The high-resolution TEM (HR-TEM) images of Fe/$NiPS_3$ indicate the surface reconstruction after Fe introduction, and the d-spacing of 0.247 nm is recognized for the $NiPS_3$ (131) plane (Fig. 2F). The selected area electron diffraction pattern (SAED; Fig. 2G) of Fe/$NiPS_3$ identifies the (131)/(201)/(132)/(331) crystal planes of $NiPS_3$ (*23*). The element mappings in Fig. 2H and fig. S21 confirm the homogeneous Fe/Ni/P/S elemental distribution in the Fe/$NiPS_3$ nanosheets.

Figure 3A presents the x-ray diffraction (XRD) patterns of bulk $NiPS_3$, EE-$NiPS_3$, and Fe/$NiPS_3$ samples. After the electrochemical exfoliation, the EE-$NiPS_3$ sample shows an interlayer spacing expansion and the presence of C/N elements relative to bulk $NiPS_3$ (fig. S22). For Fe/$NiPS_3$, the XRD peaks at 13.9°/28.1°/31.0°/36.1°/58.2° correspond to the (001)/(002)/(130)/(131)/(004) planes of $NiPS_3$ (*29*), and no Fe-related peaks can be observed. The structure of Fe/$NiPS_3$ was further examined by Raman spectroscopy in Fig. 3B and table S1. It shows the typical E_g/A_{1g} phonon modes with slight redshifts over EE-$NiPS_3$, which may be related to the hindered vibration of the $NiPS_3$ substrate atoms due to Fe introduction (*30*). Figure 3C displays the Fourier transform infrared (FTIR) spectra of these samples, in which Fe/$NiPS_3$ exhibits a higher surface O—H vibration intensity and stronger water affinity than EE-$NiPS_3$ (*28*). Their surface states were further investigated by x-ray photoelectron spectroscopy (XPS), as shown in Fig. 3 (D and E) and figs. S23 to S25. Compared to EE-$NiPS_3$, the Ni 2p peak of Fe/$NiPS_3$ exhibits a shift of approximately −0.23 eV (Fig. 3D), indicating a reduction in the Ni valence state (*31*). The Fe 2p spectrum in Fig. 3E also suggests that two kinds of Fe^{III} coordination sites were successfully introduced into the Fe/$NiPS_3$ sample (*32*). The XRD, Raman, and XPS results have stated the Fe doping characteristic in the Fe/$NiPS_3$.

We further surveyed the valence and coordination states of Ni and Fe sites in the Fe/$NiPS_3$ using x-ray absorption fine spectroscopy (XAFS). Figure 3F shows the Ni K-edge x-ray absorption near-edge structure (XANES) spectra of Fe/$NiPS_3$. Compared to EE-$NiPS_3$, the slight downshift of the XANES edge indicates the reduced Ni valence in Fe/$NiPS_3$ (Fig. 3F, inset) (*23*), in accordance with the XPS result in Fig. 3D. The Fourier transform extended X-ray absorption fine structure (FT-EXAFS) spectra were further analyzed to study the local Ni coordination environment (Fig. 3G). Compared to EE-$NiPS_3$, the Ni—S characteristic peak shifts toward a higher R value (2.28 to 2.31 Å) in Fe/$NiPS_3$, while a lower R value

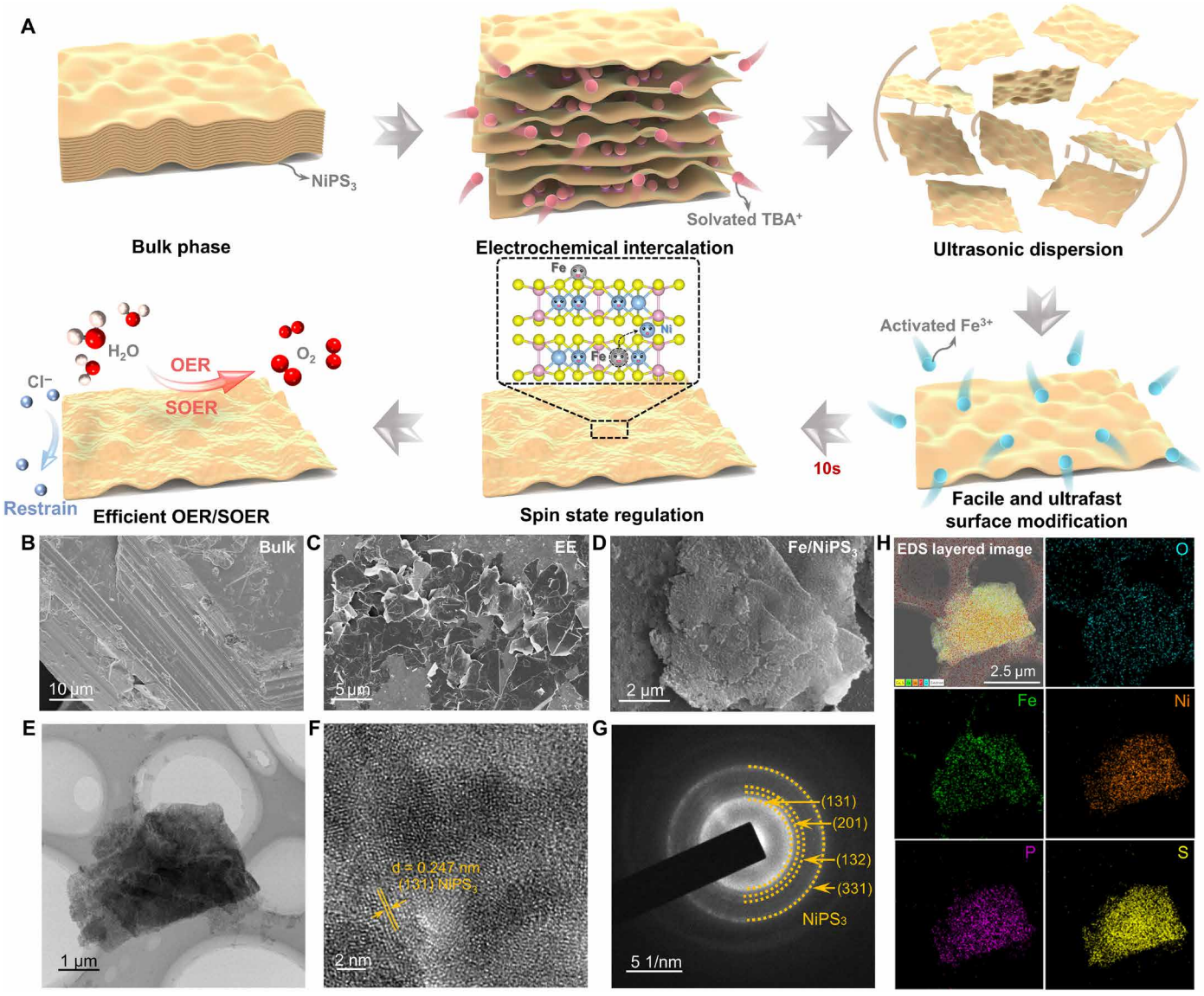

Fig. 2. Fabrication process and structural characterizations of Fe/$NiPS_3$. (**A**) The synthetic scheme; scanning electron microscopy (SEM) images of (**B**) bulk $NiPS_3$ and (**C**) EE-$NiPS_3$; (**D**) SEM image, (**E**) aberration-corrected BF-STEM image, (**F**) HR-TEM image, (**G**) SAED pattern, and (**H**) EDX mapping of Fe/$NiPS_3$.

shift (3.40 to 3.37 Å) is observed in the Ni—Ni characteristic peak. This reflects the asymmetric structure distortion of $NiPS_3$ after Fe doping. Such local active regions are prone to trigger reconstruction during the reaction process and serve as efficient evolution centers for OER intermediates. In the Fe K-edge XANES spectrum (Fig. 3H), the edge upshift relative to iron oxides reveals a decrease of electronic density and the increased Fe oxidation state in Fe/$NiPS_3$ (Fig. 3H, inset) (*28*). The Fe valence is calculated as high as +3.37 in the Fe/$NiPS_3$ material from the linear fit of XANES data (fig. S26). Therefore, the charge transfer from Fe to Ni further stabilizes the high-valence and active Fe ions, which have more unfilled orbitals and potential spin states. Through the comparison of theoretical Fe-doped $NiPS_3$ crystal structures, it is revealed that the coordination environments of Fe—S and Fe—Fe bonds have been generated in the Fe/$NiPS_3$ sample (Fig. 3I) (*33*, *34*). This result indicates that Fe has been successfully introduced into the composite structure. The changes in a coordination environment and bond length are further demonstrated with wavelet transform of the k^3- weighted EXAFS signal (figs. S27 and S28). Relative to EE-$NiPS_3$ (fig. S27A), the Fe/$NiPS_3$ is observed with stretched Ni—S and shortened Ni—Ni bonds (fig. S27B). The Fe in the Fe/$NiPS_3$ structure exhibits the Fe—S and Fe—Fe coordination, which is distinct from pure Fe foil (fig. S28). It reflects that Fe exists in a doped form without Fe metallic cluster in the composite structure. The Fe- doped $NiPS_3$ structure with asym-metric coordination and high valence would be beneficial for the efficient oxygen evolution electrocatalysis.

Catalytic properties for water oxidation

After loading on planar glassy carbon electrodes, the OER catalytic properties of different samples were evaluated in a 1 M KOH electrolyte (Fig. 4, A and B). The Fe/$NiPS_3$-4 catalyst can deliver the OER with low overpotential (η_{10}, at 10 mA cm^{-2}) of 242 mV and a

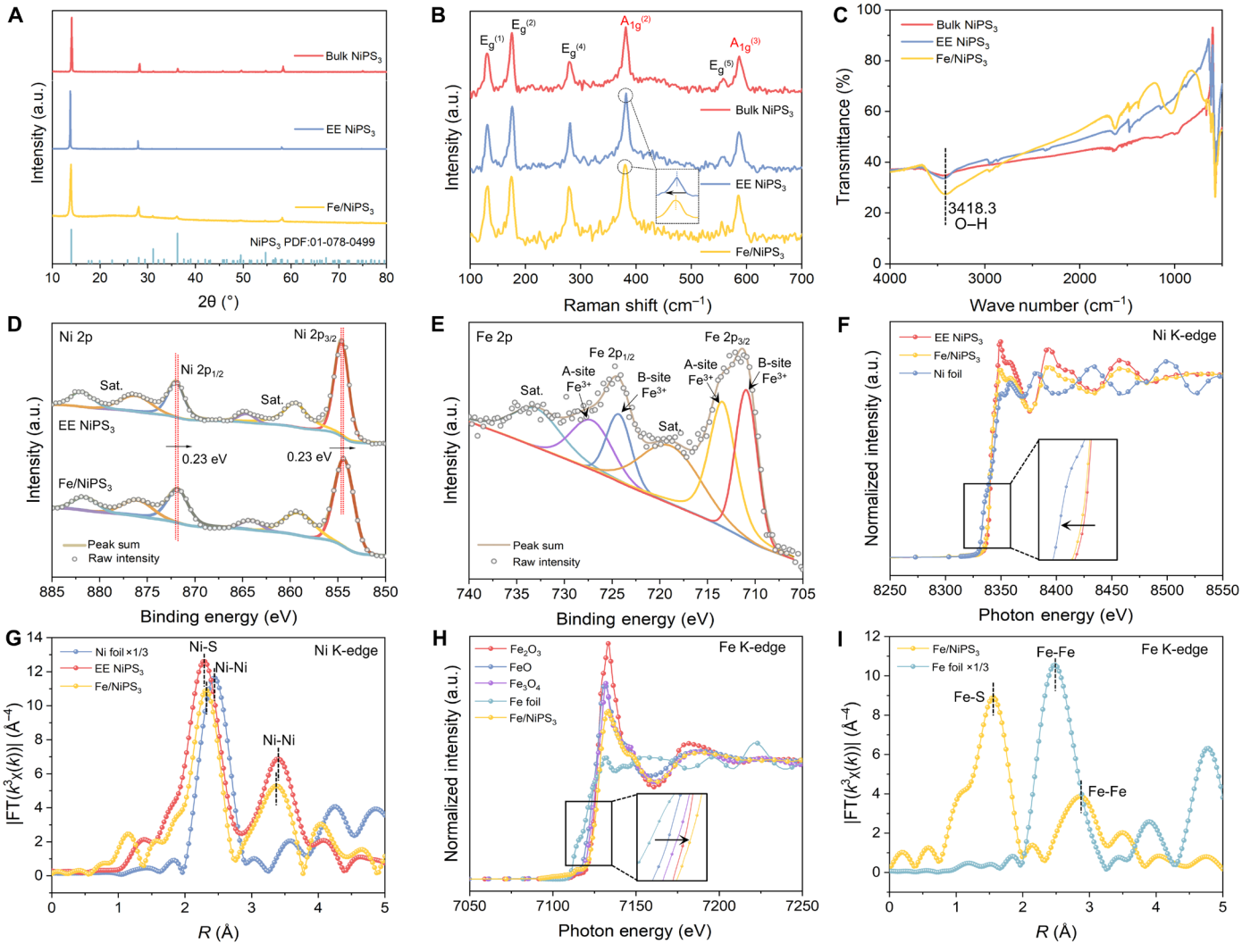

Fig. 3. Phase, electronic, and coordination structure of Fe/NiPS$_3$. (**A**) XRD patterns, (**B**) Raman spectra, and (**C**) FTIR spectra of bulk NiPS$_3$, EE-NiPS$_3$, and Fe-NiPS$_3$. (**D**) Ni 2p XPS spectra of EE-NiPS$_3$ and Fe/NiPS$_3$. (**E**) Fe 2p XPS spectrum of Fe/NiPS$_3$. (**F**) Ni K-edge XANES spectra of EE-NiPS$_3$, Fe/NiPS$_3$, and Ni foil. (**G**) Ni K-edge Fourier transform extended X-ray absorption fine structure (FT-EXAFS) spectra of EE-NiPS$_3$, Fe/NiPS$_3$, and Ni foil. (**H**) Fe K-edge XANES spectra of Fe_2O_3, FeO, Fe_3O_4, Fe/NiPS$_3$, and Fe foil. (**I**) Fe K-edge FT-EXAFS spectra of Fe/NiPS$_3$ and Fe foil. a.u., arbitrary units. PDF, powder diffraction file.

small Tafel slope of 78.1 mV dec^{-1} without Ohmic drop (iR) compensation. This performance surpasses other control samples, such as bulk NiPS$_3$ (402 mV, 134.4 mV dec^{-1}), EE-NiPS$_3$ (340 mV, 155.0 mV dec^{-1}), RuO_2 (338 mV, 120.5 mV dec^{-1}), and other ratio-synthesized Fe/NiPS$_3$ materials. After applying 80% iR compensation, the Fe/NiPS$_3$ system exhibits a low η_{10} potential of 237 mV and a small Tafel slope of 59.1 mV dec^{-1} (fig. S29). Moreover, the catalytic activity and kinetics of Fe/NiPS$_3$ powder can race with the now advanced nonprecious OER catalysts (Fig. 4C and tables S2 and S3) (*35*). We further compare the OER behaviors of different metal-doped NiPS$_3$ materials (fig. S30), among which the Fe/NiPS$_3$ performs better than other metal (e.g., Ni, Co, and Mo) doped NiPS$_3$ catalysts. When Fe/NiPS$_3$ powder is loaded on three-dimensional Ni foam, it can reach a remarkably low η_{10} of only 178 mV for OER (fig. S31); but we insist on evaluating the real and intrinsical OER behaviors on planar glassy carbon electrodes in this work (*36*). The electrochemical impedance spectroscopy (EIS) data in Fig. 4D further indicate the lowest R_{ct} in Fe/NiPS$_3$ toward the best electron transfer property among different samples. The Fe/NiPS$_3$ electrocatalyst is also revealed with higher double-layer capacitance (C_{dl}, 1.21 mF cm^{-2}; fig. S32) and an electrochemical active surface area (ECSA) for OER (*37*). It also undertakes stable OER activity for 35 hours of operation, owing to the well-maintained nanosheet morphology and elements (fig. S33). The postmortem XPS observation in fig. S31C reflects the appearance of Ni^{3+} species possibly due to the surface-reconstructed NiOOH in alkaline OER.

To evaluate the OER behaviors in seawater (SOER), we first conducted the catalytic tests in an alkaline electrolyte containing NaCl (figs. S34 and S35). It is found that the OER activity and kinetics of Fe/NiPS$_3$ in simulated seawater were not notably weakened relative to those in an alkaline electrolyte (Fig. 4, A and B). Furthermore, the SOER catalysis was assessed in an electrolyte prepared by seawater (from Bohai Sea) mixed with 1 M KOH, as shown in Fig. 4E. The Fe/NiPS$_3$ electrocatalyst presents the low η_{10} of 264 mV and a small

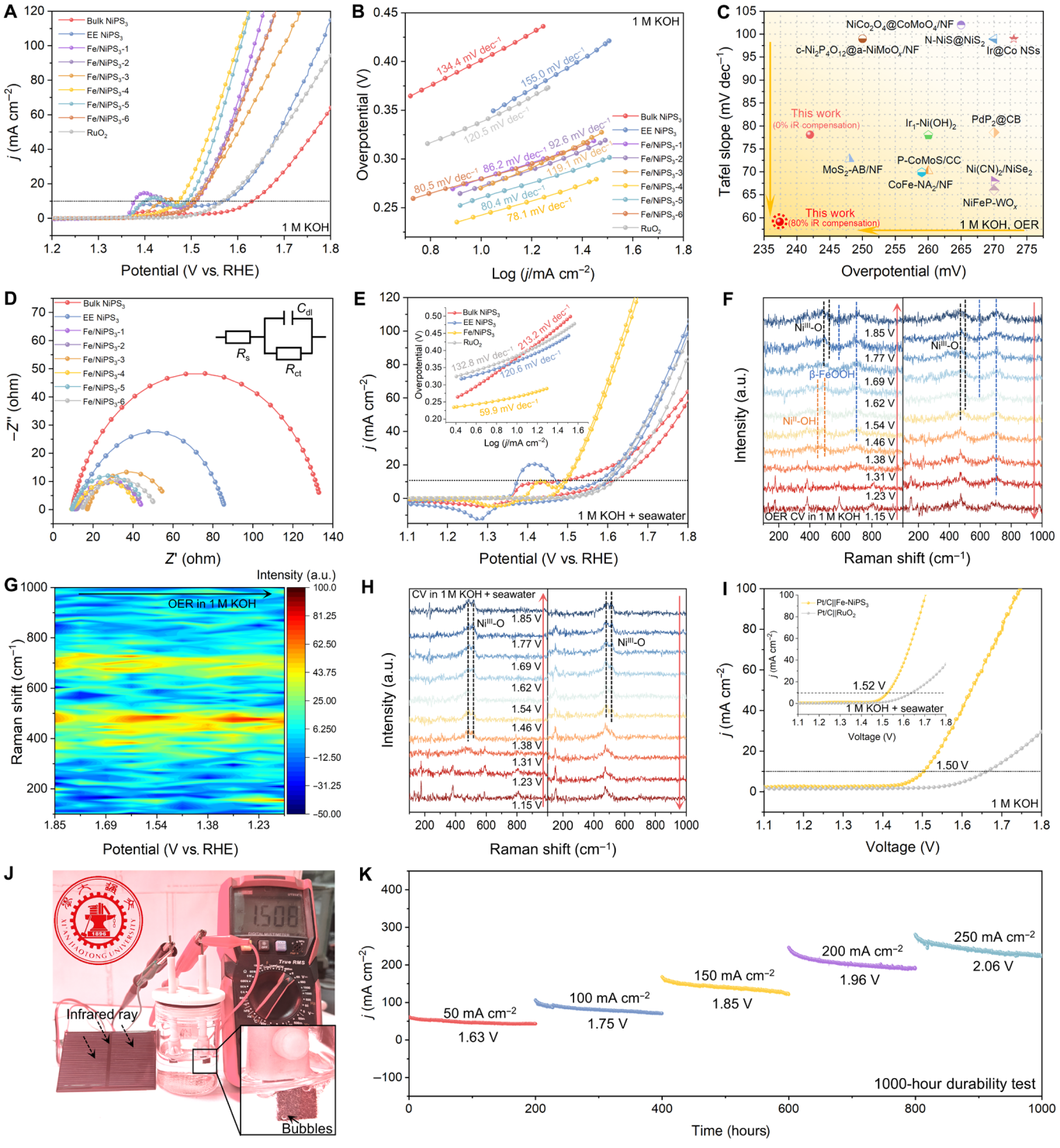

Fig. 4. Electrocatalytic properties of different catalysts. (**A**) LSV curves, (**B**) Tafel plots, and (**C**) performance comparison with recently reported catalysts. (**D**) EIS data, and the inset shows the fitting circuit (R_{ct}: charge-transfer resistance; R_s: ohmic resistance; C_{dl}: double-layer capacitance). (**E**) CV curves (inset, Tafel plots) in 1 M KOH with seawater for OER. (**F**) The in situ Raman spectra of Fe/$NiPS_3$ at different applied potentials versus RHE in 1 M KOH. (**G**) The corresponding two-dimensional projection mapping of the reverse scanning curves in (F). (**H**) The in situ Raman spectra in 1 M KOH with seawater. (**I**) Polarization curves of WE based on Pt/C||Fe/$NiPS_3$ couple in 1 M KOH (inset, in 1 M KOH with seawater). (**J**) Photograph of the WE device driven by a solar cell (~1.5 V). (**K**) *i-t* Measurement of the Pt/C||Fe/$NiPS_3$ couple for 1000-hour WE. a.u., arbitrary units.

Tafel slope of 59.9 mV dec^{-1}, which is superior to EE-$NiPS_3$ (370 mV, 120.6 mV dec^{-1}) and commercial RuO_2 (384 mV, 132.8 mV dec^{-1}). The corresponding EIS experiment also indicates the faster electron transfer for SOER (fig. S36). After 20 hours of SOER testing, the catalyst also showed considerable activity and a retention of sheet-like structure and Ni/Fe/P/S elements; the generation of similar Ni^{3+} species also reveals possible surface reconstruction (fig. S37). In situ Raman spectroscopy was used to monitor the structural evolution during actual OER processes (Fig. 4, F to H, and figs. S38 and S39). In 1 M KOH (Fig. 4, F and G, and fig. S38), additional Raman peaks appeared for Fe/$NiPS_3$ within a complete OER cyclic voltammetry (CV) cycle. It indicates that the Fe/$NiPS_3$ surface is initially reconstructed to Ni^{II}-OH species (from ~1.46 V, 449.3 cm^{-1}, 496.8 cm^{-1}), followed by the formation of Ni^{III}-O (from ~1.77 V, 489.8 cm^{-1}, 544.1 cm^{-1}) and β-FeOOH (from ~1.46 V, 592.8 cm^{-1}, 686.1 cm^{-1}) (*38*–*40*). In addition, there was no emergence of additional P- and S-related Raman vibration modes. As the uniform P/S distribution in the post-OER elemental analyses (fig. S33), it can be reasonably inferred that the Fe/$NiPS_3$ system lastly forms a P/S-doped NiOOH/FeOOH heterostructure. While in seawater, only NiOOH was observed from in situ Raman tests (Fig. 4H and fig. S39), and Fe/P/S elements are uniformly distributed after SOER (fig. S37). This accounts Fe/P/S-doped NiOOH structure as the actual SOER active species. Further XRD and Raman characterizations of the products after the reactions also confirmed these views (fig. S40). The Fe/$NiPS_3$ precatalyst is also found with superior catalytic performance to the precatalyst NiFe layered double hydroxides (NiFe-LDH; fig. S40) and previous reported NiFe oxyhydroxides (*41*, *42*). This indicates the advantageous role of P/S coordination in improving the performance of the Fe—Ni couple. Similarly, the performance of the precatalyst NiFe-LDH is superior to that of the $Ni(OH)_2$ and $Fe(OH)_3$ precatalysts (fig. S41). It also suggests that the Fe—Ni configuration is more favorable for OER catalysis compared to the Ni—Ni and Fe—Fe couples, as consistent with the spin state calculations (fig. S5C). Besides, NiFe-LDH exhibits the smallest R_{ct} and the fastest charge transfer efficiency (fig. S41E), which aligns with the theoretical charge transfer characteristics (Fig. 1G and fig. S8).

A Pt/C||Fe/$NiPS_3$ electrode pair was constructed to evaluate WE performance, exhibiting a low cell η_{10} voltage of 1.50 V (Fig. 4I). To demonstrate practical applications in sustainable hydrogen production, a solar power–assisted WE device was designed and shown in Fig. 4J. With the infrared photovoltaic (~1.5 V) electrolyzer, bubbles were visible on the surfaces of both electrodes. This electrode pair could also stably operate for more than 1000 hours at varied current densities for alkaline WE by applying different voltages (Fig. 4K). We further evaluated the WE performance in seawater for the Pt/C||Fe/$NiPS_3$ couple (Fig. 4I, inset), which achieved a low η_{10} of 1.52 V and a good durability over 100 hours (fig. S42). Contact angle measurements in fig. S43 confirm the better hydrophilicity and stronger water activation capacity of the Fe/$NiPS_3$ structure (*23*). The above results indicate that the transition metal-based Fe/$NiPS_3$ catalyst can play an active role in sustainable WE applications.

Localized spin state adaptation of Fe/$NiPS_3$

The local spin state of the Fe/$NiPS_3$ system was further investigated to gain insights into the enhanced OER behaviors. Electron spin resonance (ESR) spectroscopy was applied to inspect the presence of unpaired electrons, as shown in Fig. 5A. The Fe/$NiPS_3$ is observed with much higher peak intensity than that of EE-$NiPS_3$, ascertaining the active role of Fe doping in the increase of unpaired electrons (*43*). Similar ESR signals between pristine Fe/$NiPS_3$ and after-OER sample (Fe/$NiPS_3$-A) can reflect the slight change of unpaired electron number during OER. We further studied their magnetism by superconducting quantum interference device measurements. As displayed with magnetic hysteresis loops (Fig. 5B), the slopes of Fe/$NiPS_3$ and Fe/$NiPS_3$-A are larger than that of EE-$NiPS_3$, indicating the enhanced magnetism and the altered spin state after Fe incorporation.

For further experimental evidence of spin adaptation, temperature-dependent magnetization measurements were carried out from 2 to 300 K under zero-field cooling (ZFC) and field cooling (FC) conditions at 1000 Oe (Fig. 5, C and D). The graphs show that the magnetization curves of Fe/$NiPS_3$ under ZFC and FC conditions partially overlap throughout the entire temperature range, while $NiPS_3$ completely overlaps. Figure S44 shows the plots of the reciprocal of magnetization against temperature. The $1/\chi$ intercept (Curie-Weiss temperature, θ) of EE-$NiPS_3$ is a negative value with a very small magnetization, demonstrating its AFM nature (*44*). For Fe/$NiPS_3$ (fig. S31B), there is a critical temperature T_c greater than 0 K (27.0 K), indicating that it may exhibit ferromagnetism at low temperatures. This result further demonstrates that the introduction of Fe causes a change in spin magnetic state. The effective magnetic moment (μ_{eff}) of each sample was evaluated by fitting the slope of the inverse magnetization curve with the Curie-Weiss equation (Fig. 5, E and F). The μ_{eff} of Fe/$NiPS_3$ at RT (4.29 μ_B) is higher than the μ_{eff} of EE-$NiPS_3$ (1.76 μ_B), illustrating that Fe induces a higher spin state in Fe/$NiPS_3$ relative to EE-$NiPS_3$. According to the equation $\mu_{eff} = \sqrt{n(n+2)}\mu_B$, the number of unpaired electrons (n) was evaluated as ~1.0 and ~3.4 for $NiPS_3$ and Fe/$NiPS_3$ at RT, respectively. The introduction of Fe brings more unpaired electrons in Fe/$NiPS_3$.

Moreover, the ^{57}Fe Mössbauer spectroscopy was performed to distinguish different iron spin species (Fig. 5G and fig. S45), and the spectra were fitted with two quadrupole doublets (D1 and D2). In fig. S45, the same isomer shift (IS; ~0.34 mm s^{-1}) proves that two doublets belong to the same Fe^{III} valence state, while the different quadrupole splitting (QS; 0.53 mm s^{-1} for D1 and 0.94 mm s^{-1} for D2) means various coordinations (*45*). Combined with IS and QS values, the D1/D2 doublets are attributed to the tetrahedral/octahedral (A/B site) Fe^{III} with MS/HS states, respectively (*32*, *46*, *47*). The content of D1 (MS Fe^{III}) increased from 60.25 to 72.32% in Fe/$NiPS_3$ after the OER reaction (Fig. 5G). In situ x-ray emission spectroscopy (XES) measurements were further conducted to evaluate the Fe spin state evolution during OER (Fig. 5H and fig. S46). Note that the relative intensity of the Kβ' characteristic peak depends on the number of unpaired 3d electrons (*48*). In 1 M KOH and seawater, as the voltage gradually increases, the local spin states of Fe are observed to decrease, which is consistent with the results of Mössbauer spectroscopy (*49*). Thus, the MS Fe^{III} site is considered to become a dominant center along the OER process. Echoing the previous structure/performance analyses, the localized spin results further confirm the essential role of MS Fe^{III} site in the OER efficiency enhancement (Fig. 5I).

AEMWE/AEMSWE electrolysis measurements

To verify the actual performance of Fe/$NiPS_3$, we assembled it in an anion exchange membrane water electrolyzer (AEMWE). Figure 6 (A and B) illustrates the schematic setup and digital photograph. First, we examined the AEMWE performance using a 1 M KOH

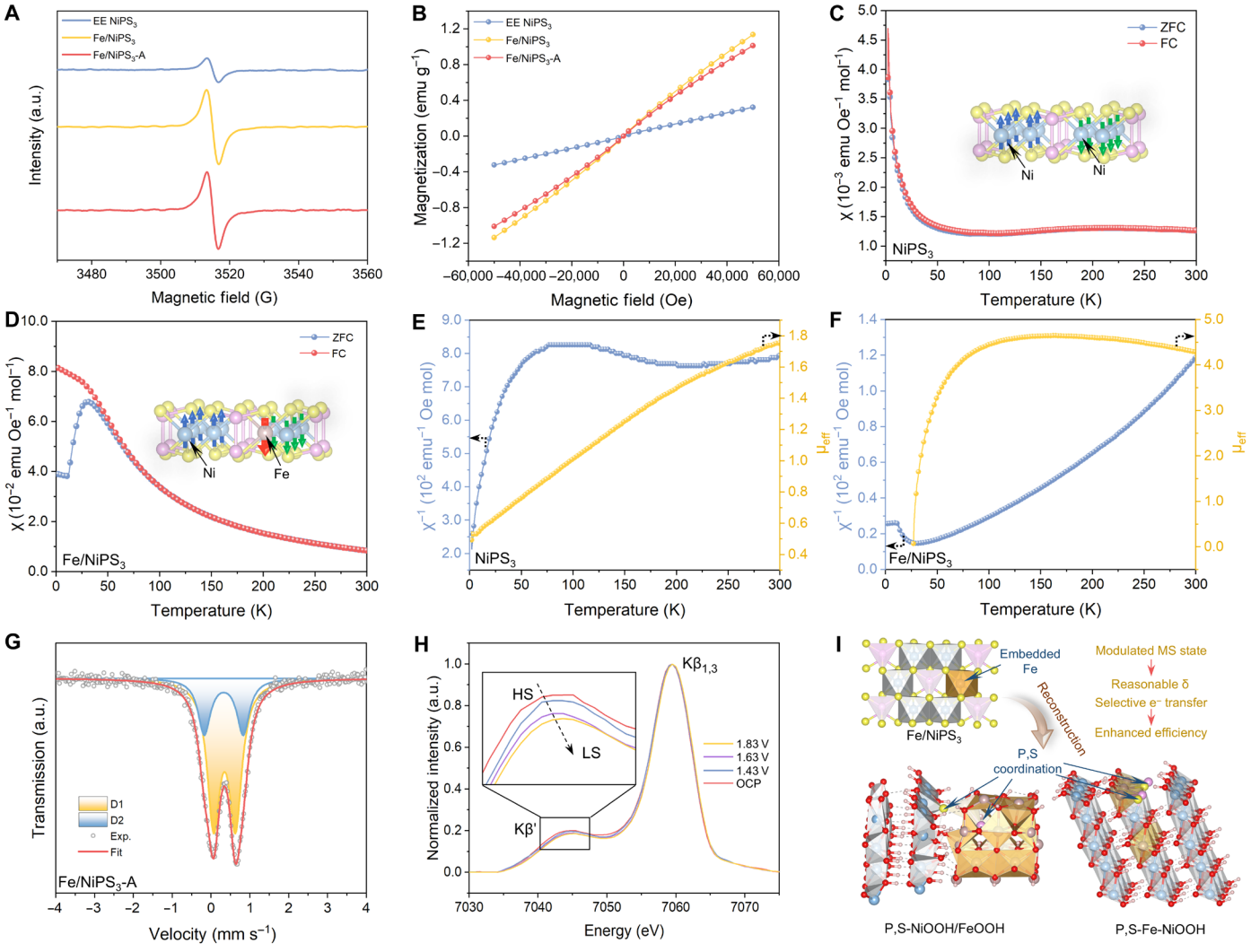

Fig. 5. Localized spin state analyses for Fe/NiPS$_3$-based catalysts. (**A**) ESR spectra of the EE-NiPS$_3$, Fe/NiPS$_3$, and Fe-NiPS$_3$-A. (**B**) Hysteresis curves of EE-NiPS$_3$, Fe/NiPS$_3$, and Fe-NiPS$_3$-A. FC and ZFC susceptibility plotted versus temperature for (**C**) EE-NiPS$_3$ and (**D**) Fe/NiPS$_3$. χ^{-1} plots and the μ_{eff} curves for (**E**) EE-NiPS$_3$ and (**F**) Fe/NiPS$_3$. (**G**) Mössbauer transmission spectra of Fe/NiPS$_3$-A. (**H**) In situ Fe Kβ XES spectra of Fe/NiPS$_3$ during OER in 1 M KOH. (**I**) Schematic diagram of localized spin state modulation for enhancing OER catalytic activity. emu, electromagnetic unit; LS, low spin. a.u., arbitrary units. OCP, open circuit potential.

electrolyte. The cell voltage measured at RT with Pt/C||Fe/NiPS$_3$ was lower than that of Pt/C||RuO$_2$ under the same current density (Fig. 6C). By heating the electrolyte, the cell demonstrated improved alkaline WE performance. At 45°C, Pt/C||Fe/NiPS$_3$ and Pt/C||RuO$_2$ required only 1.73 and 3.24 V to achieve a current density of 0.5 A cm^{-2}, respectively. Further, the anion exchange membrane seawater electrolyzer (AEMSWE) performance was tested using 1 M KOH + seawater electrolyte. Compared to other components, Pt/C||Fe/NiPS$_3$-45°C also exhibited optimal performance with a low cell voltage of 1.79 V at 0.5 A cm^{-2} (Fig. 6D). Besides, the electrolyzer remained stable for 100 to 200 hours at RT under the current density of 0.2 A cm^{-2}, with a performance degradation of less than 3% (Fig. 6, E and F). It is worth noting that the activity of the Fe/NiPS$_3$ anode catalyst in AEM(S)WE remains comparable to many state-of-the-art electrodes (Fig. 6G). The active and durable performance of Fe/NiPS$_3$ empowers its application as a suitable anode catalyst for membrane electrode assembly (MEA) devices.

Detailed insights for the enhanced catalytic mechanism

Thermodynamic calculation was further conducted to underlie the spin-boosted catalytic mechanism in water oxidation. As previously mentioned, for Ni/Fe oxyhydroxide bulk phase (figs. S3 and S4), Fe heteroatom can break the symmetry of tacticity and the equilibrium of local spin state, possibly leading to the generation of surplus spin polarons around the heteroatom. As shown in fig. S47, the Fe incorporation enriches the electronic states in the conduction band above the Fermi level to promote electron transfer (*8*). Besides, the amount of Fe doping must be controlled in the system to prevent the semiconductor transformation and conductivity reduction.

Furthermore, the model of P/S-NiOOH/FeOOH was constructed on the basis of previous in situ Raman, XRD, and post-OER results to simulate the OER catalytic behavior. First, we evaluated the formation energies of NiOOH/FeOOH with different heterointerface coupling configurations and selected the most stable NiOOH-(001)/FeOOH-(001) configuration as the substrate (figs. S48 and S49). The

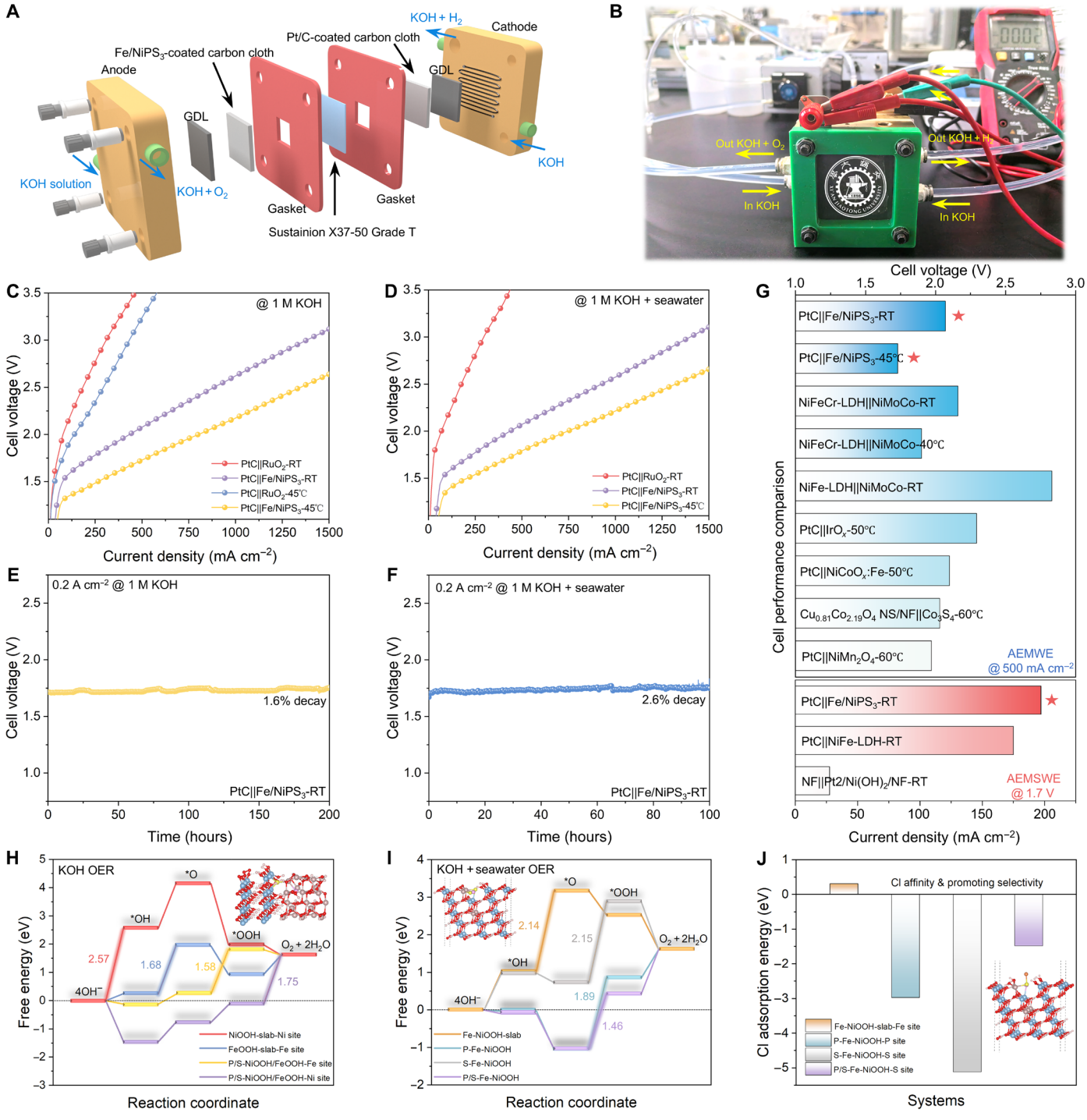

Fig. 6. AEMWE device performances and the enhanced OER mechanism studies. (**A**) Schematic structure diagram and (**B**) the photograph of the AEMWE device. (**C**) Cell voltages of Pt/C||RuO_2 at RT, Pt/C||$Fe/NiPS_3$ at RT, Pt/C||RuO_2 at 45°C, and Pt/C||$Fe/NiPS_3$ at 45°C at different current densities for AEMWE without iR compensation in a 1 M KOH electrolyte. (**D**) Cell voltages of Pt/C||RuO_2 at RT, Pt/C||$Fe/NiPS_3$ at RT, and Pt/C||$Fe/NiPS_3$ at 45°C under different current densities for AWE without iR compensation in a 1 M KOH + seawater electrolyte. Long-term stability of Pt/C||$Fe/NiPS_3$ at RT/0.2 A cm^{-2} (**E**) for 200 hours in a 1 M KOH electrolyte and (**F**) for 100 hours in a 1 M KOH + seawater electrolyte. (**G**) Cell performance comparison between as-prepared electrodes and other reported electrodes; here, the top part compares the cell voltages at 500 mA cm^{-2} in AEMWE, and the bottom part compares the current density at 1.7 V in AEMSWE. Energy barriers for four-electron–step OER process in (**H**) KOH and (**I**) KOH + seawater (pH = 14, $U = 0$ eV). (**J**) Cl adsorption energy at different sites.

P/S coordination with Fe was applied to typically illustrate their regulation effects on the Fe spin state (fig. S50A). The spin density characterization in fig. S50B revealed the presence of lower spin Fe near the interface (Fe^{interf}) and higher spin Fe inside the FeOOH (Fe^{bulk}). The spin state manifests a further decrease for the P/S-coordinated interfacial Fe site ($Fe^{P/S}$). Combined with XPS and Mössbauer spectra results (Figs. 3E and 5G), Fe^{bulk} is supposed to be in HS state due to its coordination with more weak-field ligands like OH, while the less OH-coordinated Fe^{interf} and P/S-coordinated $Fe^{P/S}$ are mostly in the MS states (*50*). It is worth noting that nonmetallic atoms (e.g., S) at the NiOOH/FeOOH interface also exhibit the same spin direction with the neighboring Ni and Fe atoms (fig. S50B), which is also applicable to the aforementioned SSETC protocol. Overall, the spin state of Fe in the P/S-NiOOH/FeOOH is regulated by the coupling of the interface and P/S atoms, promoting electron transport in the OER process (fig. S51). The widely accepted adsorbate evolution mechanism was applied to evaluate the thermodynamic process of alkaline OER (Supplementary Text and figs. S52 to S55). In addition, the theoretical OER overpotentials (η) are listed in table S4. Relative to the Ni site in pure NiOOH slab, the Fe site in P/S-NiOOH/FeOOH can exhibit better *OH adsorption and moderate step energy of *O → *OOH (Fig. 6H), resulting in the lowest η (1.18 eV). We also considered other distribution schemes of P/S doping (fig. S56). In all cases, the Fe—Ni couple at the interface can form an SSETC with the same spin direction, and the P/S dual coordination further stabilizes the MS state of Fe. These results suggest that the Fe site serves as the actual active center during OER and underscores the necessity of local spin state adaptation.

Considering seawater environments, we also profiled the models of Fe-NiOOH slab in fig. S41 based on the previous in situ Raman results (Fig. 4H). Relative to NiOOH slab, the introduction of Fe notably affects the local spin state due to the tacticity asymmetry (fig. S57, A to F). Specifically, the Fe^{surf} site in Fe-NiOOH exhibits a lower Fe^{III} spin state than the Fe^{bulk} site (fig. S57, G and H). Various P-, S-, and P/S-doped Fe-NiOOH systems were constructed to investigate the necessity of P/S codoping in enhancing Fe site activity (fig. S58). The Fe^{surf} site with P/S coordination is also inferred to be in the MS state, while the Fe^{bulk} site is in the HS state (*50*). It is also found that the P/S dual coordination can present a larger decrease of Fe^{surf} spin state than that of single P or S coordinated case. As a result, thermodynamic analysis (figs. S59 to S62 and table S5) confirmed the lowest RDS energy and the smallest η value (1.06 eV) for the Fe site in P/S-Fe-NiOOH (Fig. 6I). In addition, the effects of a pH value and electrode potential were profiled in figs. S63 and S64, indicating the optimal activities of Fe sites in the P/S-Fe-NiOOH and P/S-NiOOH/FeOOH systems. The solvent influence was further considered by adding explicit and implicit solvation models (*51*–*53*). It was observed that solvation did not cause notable changes in the spin state and the optimal catalytic sites of the system (figs. S65 to S67). Compared to the pure Fe-NiOOH system, the dual-doped P/S sites have strong adsorption effect on Cl^-, inhibiting its accumulation at Fe active sites (Fig. 6J, figs. S68 and S69, and table S6) (*54*). Therefore, the synergy of P/S sacrificial sites and Fe active centers can suppress the occurrence of ClOR and improve the OER selectivity in seawater electrolysis.

DISCUSSION

To summarize, we have theoretically and experimentally profiled the necessity of localized spin state adaptation in promoting OER/SOER with the asymmetric Fe/$NiPS_3$ system. It is indicated that the MS Fe^{III} site can grant the evolution of OER intermediates more energetically. As a result, the Fe/$NiPS_3$ structure has achieved superior alkaline OER performance over RuO_2, with a low η_{10} potential of 242 mV and fast kinetics. In the reconstructed structure, the synergy of Fe active centers with P/S sacrificial sites inhibits the ClOR toward selective and durable OER catalysis, presenting excellent SOER performance with a low η_{10} potential of 264 mV. The optimized Pt/C||Fe/$NiPS_3$ electrode couple demonstrated low cell voltages of 1.50 V for OWS and 1.52 V for SOWS at 10 mA cm^{-2}, together with a stable operation for 1000 hours. As in the practical AEM(S)WE devices, the electrode couple showcases a voltage of only 1.73 V to achieve a current density of 0.5 A cm^{-2} at 45°C. Combined with DFT calculations, ESR, ZFC, and Mössbauer spectroscopy, we have deciphered the enhancement mechanism of OER activity/selectivity on the spin regulation of Fe active sites. This research puts forward an effective asymmetric strategy to relevel the localized metal spin state for highly efficient (sea)water oxidation electrocatalysis.

MATERIALS AND METHODS

Electrochemical exfoliation of $NiPS_3$

The fabrication of $NiPS_3$ crystals was achieved through the conventional chemical vapor transport method (*55*). Subsequently, an electrochemical workstation (Autolab PGSTAT204) was used to perform electrochemical exfoliation in a two-electrode configuration (Pt wire as the counter electrode and bulk $NiPS_3$ as the working electrode). The electrolytic solution was produced by dissolving 0.05 M tetrabutylammonium tetrafluoroborate (98%) in 30 ml of *N*,*N*′-dimethylformamide (99.5%). Throughout the exfoliation procedure, a constant bias voltage of −5 V was applied to the working electrode, resulting in a brown suspension. This suspension was subsequently exposed to an ice bath ultrasonic process at 300 W for 90 min to further disperse the $NiPS_3$ nanosheets. The resulting material was washed with ethanol five times to eliminate the residual exfoliation electrolyte on the surface of nanosheets and then dried under vacuum at 60°C overnight to yield EE-$NiPS_3$ powder.

Synthesis of Fe/$NiPS_3$

First, 20 mg of EE-$NiPS_3$ powder was ultrasonically dispersed in 5 ml of deionized water to obtain suspension A. Second, a preheated aqueous solution containing Fe^{3+} ions was prepared: Iron(III) chloride hexahydrate (0.101 g, 0.37 mmol) and sodium nitrate (0.212 g, 2.49 mmol) were dissolved in 45 ml of deionized water and kept at 100°C under the protection of argon for at least 5 min to obtain a deep orange solution B. Then, the preheated suspension A was quickly injected into solution B and kept for 10 s at 100°C. Last, Fe/$NiPS_3$ powder was obtained by washing the product with deionized water/ethanol several times and drying overnight under vacuum at 60°C. For comparison, a series of Fe/$NiPS_3$ materials with different element ratios was prepared when adjusting the Fe^{3+} concentration in the preheated solution. The sample prepared with 0.37 mmol of iron(III) chloride hexahydrate and 2.49 mmol of sodium nitrate was named Fe/$NiPS_3$-4. The samples with the same proportion to decrease the raw material iron(III) chloride hexahydrate/sodium nitrate to 0.09 mmol/0.62 mmol, 0.19 mmol/1.25 mmol, and 0.28 mmol/1.87 mmol were named as Fe/$NiPS_3$-1, Fe/$NiPS_3$-2, Fe/$NiPS_3$-3, respectively. The samples with the same proportion to increase the raw material iron(III) chloride hexahydrate/sodium

nitrate to 0.46 mmol/3.11 mmol and 0.56 mmol/3.74 mmol were named as Fe/$NiPS_3$-5 and Fe/$NiPS_3$-6, respectively.

Material characterization

XRD patterns were procured using a λ = 1.54056 Å Cu Kα1 radiation source via a PANalytical X'Pert Pro diffractometer. The analysis of micrographic imagery was conducted by a field emission scanning electron microscope (FEI Verios460). Using JEOL JEM-F2100, the TEM images were captured to study the morphologies and microstructures. Thermo Fisher Spectra 300 microscopy, functioning at 300 kV, was used to capture double spherical aberration-corrected TEM images, high-angle annular dark-field STEM images, and energy-dispersive spectroscopic elemental mapping. LabRAM HR Evolution was used to capture Raman spectra with a 532-nm laser serving as an excitation source. The presence of functional groups on the samples was examined using an FTIR spectrometer (IRPrestige-21). XPS analysis was conducted using Thermo Fisher Scientific ESCALAB Xi+. Measurements of XAFS were executed with a synchrotron radiation source using a Si (111) monochromator crystal at the BL14B2 beamline at SPring-8, in Japan. All XAFS experiments were recorded in transmission mode at RT, and the data were analyzed using Athena software (*56*). The optical contact angle was measured using Kruss DSA30 equipment. The M-H curve was measured by Quantum Design/MPMS3, with a magnetic field range of −50,000 to 50000 Oe and a step size of 4000 Oe. ZFC and FC measurements were measured using Quantum Design/MPMS3. Samples were cooled down to 2 K via a cryocooler-based cooling system at zero fields. Then, an external field of 1000 Oe was applied, and the samples were heated to 300 K at 5 K/min. The atomic force microscope image was acquired using a Bruker ICON instrument. XES was carried out using the Rapid XES (Anhui Absorption Spectroscopy Analysis Instrument Co. Ltd.) at 25 kV and 3 mA, and the Ge (620) spherically bent crystal analyzer with a radius of curvature of 500 mm was used for Fe.

Electrochemical measurements

The catalyst ink formulation involved the dispersion of catalyst powder (4 mg) into a mixed solution of isopropanol (450 μl), deionized water (50 μl), and 5 wt % Nafion (20 μl). This was followed by the uniform deposition and drying of the catalytic ink (10 μl) on a glassy carbon (3 mm in diameter) working electrode. Characterization of the alkaline OER properties of various catalysts was conducted using a standard three-electrode system on the Autolab PGSTAT204 workstation, equipped with a graphite rod counter electrode and a Hg/HgO reference electrode in 1 M KOH. For the electrolysis of seawater, the OER properties of the catalyst were studied not only in simulated seawater (1 M KOH + 0.5 M NaCl and 1 M KOH + 1 M NaCl) but also in natural seawater (1 M KOH + Bohai seawater). The linear sweep voltammetry (LSV) curve was scanned at a speed of 5 mV s^{-1}, with a potential range of 1.2 to 1.8 V versus reversible hydrogen electrode (RHE) for OER. Before the LSV test, each electrode underwent 20 cycles of CV testing at a scan rate of 100 mV s^{-1}. Charge transfer resistance (R_{ct}) was fitted through EIS measurements, applying an alternating current voltage (amplitude of 5 mV) in the frequency range of 100 kHz to 0.1 Hz. For the ECSA testing, the electrochemical double-layer capacitance (C_{dl}) was assessed on the basis of the CV test under the potential window of 1.11 to 1.21 V (versus RHE), with scan rates of 20, 40, 60, 80, 100, and 120 mV s^{-1}. All tests were reiterated two to four times to ensure reproducibility. The overall water splitting performance was studied using a two-electrode device in 1 M KOH or a seawater electrolyte. The LSV polarization curve was measured within the range of 1.1 to 1.8 V (versus RHE) at a scan speed of 5 mV s^{-1}. Chronopotentiometry was used to gauge long-term catalytic stability. Except for special instructions in the text, all other data have not been compensated by iR.

AEMWE/AEMSWE tests

For water electrolyzer testing, we assembled a unit battery with 2 cm–by–2 cm MEA. Fe/$NiPS_3$-coated carbon cloth was used as the anode catalytic layer, and commercial 20% Pt/C-coated carbon cloth was used as the cathode catalytic layer. Ti fiber felt was used as the gas diffusion layer. A Sustainion X37-FA anion exchange membrane was clamped between the cathode and the anode. The flowing electrolyte solution was 1 M KOH or 1 M KOH + seawater, and its temperature can be controlled at RT or 45°C through a water bath and heated electrode plates. Electrochemical testing was conducted at a set temperature, and the current density–voltage relationship was obtained without any iR correction.

Supplementary Materials

This PDF file includes:

Supplementary Text
Figs. S1 to S69
Tables S1 to S6
References

REFERENCES AND NOTES

1. E. T. Vogt, B. M. Weckhuysen, The refinery of the future. *Nature* **629**, 295–306 (2024).
2. L. Chong, G. Gao, J. Wen, H. Li, H. Xu, Z. Green, J. D. Sugar, A. J. Kropf, W. Xu, X.-M. Lin, H. Xu, L. W. Wang, D. J. Liu, La-and Mn-doped cobalt spinel oxygen evolution catalyst for proton exchange membrane electrolysis. *Science* **380**, 609–616 (2023).
3. Z. Pei, H. Zhang, Z.-P. Wu, X. F. Lu, D. Luan, X. W. Lou, Atomically dispersed Ni activates adjacent Ce sites for enhanced electrocatalytic oxygen evolution activity. *Sci. Adv.* **9**, eadh1320 (2023).
4. H. Yang, C. Dong, H. Wang, R. Qi, L. Gong, Y. Lu, C. He, S. Chen, B. You, H. Liu, J. Yao, X. Jiang, X. Guo, B. Y. Xia, Constructing nickel-iron oxyhydroxides integrated with iron oxides by microorganism corrosion for oxygen evolution. *Proc. Natl. Acad. Sci. U.S.A.* **119**, e2202812119 (2022).
5. J. Xu, H. Jin, T. Lu, J. Li, Y. Liu, K. Davey, Y. Zheng, S.-Z. Qiao, $IrO_x{\cdot}nH_2O$ with lattice water-assisted oxygen exchange for high-performance proton exchange membrane water electrolyzers. *Sci. Adv.* **9**, eadh1718 (2023).
6. L. Li, J. Zhou, X. Wang, J. Gracia, M. Valvidares, J. Ke, M. Fang, C. Shen, J. M. Chen, Y. C. Chang, C. W. Pao, S. Y. Hsu, J. F. Lee, A. Ruotolo, Y. Chin, Z. Hu, X. Huang, Q. Shao, Spin-polarization strategy for enhanced acidic oxygen evolution activity. *Adv. Mater.* **35**, e2302966 (2023).
7. Z.-Y. Wu, F.-Y. Chen, B. Li, S.-W. Yu, Y. Z. Finfrock, D. M. Meira, Q.-Q. Yan, P. Zhu, M.-X. Chen, T.-W. Song, Z. Yin, H. W. Liang, S. Zhang, G. Wang, H. Wang, Non-iridium-based electrocatalyst for durable acidic oxygen evolution reaction in proton exchange membrane water electrolysis. *Nat. Mater.* **22**, 100–108 (2023).
8. Y. Sun, S. Sun, H. Yang, S. Xi, J. Gracia, Z. J. Xu, Spin-related electron transfer and orbital interactions in oxygen electrocatalysis. *Adv. Mater.* **32**, e2003297 (2020).
9. Z. Sun, L. Lin, J. He, D. Ding, T. Wang, J. Li, M. Li, Y. Liu, Y. Li, M. Yuan, B. Huang, H. Li, G. Sun, Regulating the spin state of Fe^{III} enhances the magnetic effect of the molecular catalysis mechanism. *J. Am. Chem. Soc.* **144**, 8204–8213 (2022).
10. T. Sun, Z. Tang, W. Zang, Z. Li, J. Li, Z. Li, L. Cao, J. S. Dominic Rodriguez, C. O. M. Mariano, H. Xu, P. Lyu, X. Hai, H. Lin, X. Sheng, J. Shi, Y. Zheng, Y. R. Lu, Q. He, J. Chen, K. S. Novoselov, C. H. Chuang, S. Xi, X. Luo, J. Lu, Ferromagnetic single-atom spin catalyst for boosting water splitting. *Nat. Nanotechnol.* **18**, 763–771 (2023).
11. L. Li, Y. Wang, R. R. Nazmutdinov, R. R. Zairov, Q. Shao, J. Lu, Magnetic field enhanced cobalt iridium alloy catalyst for acidic oxygen evolution reaction. *Nano Lett.* **24**, 6148–6157 (2024).
12. C. Kuai, C. Xi, A. Hu, Y. Zhang, Z. Xu, D. Nordlund, C.-J. Sun, C. A. Cadigan, R. M. Richards, L. Li, C. K. Dong, X. W. du, F. Lin, Revealing the dynamics and roles of iron incorporation in nickel hydroxide water oxidation catalysts. *J. Am. Chem. Soc.* **143**, 18519–18526 (2021).

13. J. Ge, X. Ren, R. R. Chen, Y. Sun, T. Wu, S. J. H. Ong, Z. J. Xu, Multi-domain versus single-domain: A magnetic field is not a must for promoting spin-polarized water oxidation. *Angew. Chem. Int. Ed. Engl.* **62**, e202301721 (2023).
14. Z. Zhao, Y. Wang, X. Yang, J. Quan, B. C. Krüger, P. Stoicescu, R. Nieman, D. J. Auerbach, A. M. Wodtke, H. Guo, G. B. Park, Spin-dependent reactivity and spin-flipping dynamics in oxygen atom scattering from graphite. *Nat. Chem.* **15**, 1006–1011 (2023).
15. Z. Zhang, P. Ma, L. Luo, X. Ding, S. Zhou, J. Zeng, Regulating spin states in oxygen electrocatalysis. *Angew. Chem. Int. Ed. Engl.* **62**, e202216837 (2023).
16. Z. Xiong, C. Hu, X. Luo, W. Zhou, Z. Jiang, Y. Yang, T. Yu, W. Lei, C. Yuan, Field-free improvement of oxygen evolution reaction in magnetic two-dimensional heterostructures. *Nano Lett.* **21**, 10486–10493 (2021).
17. R. Fan, C. Liu, Z. Li, H. Huang, J. Feng, Z. Li, Z. Zou, Ultrastable electrocatalytic seawater splitting at ampere-level current density. *Nat. Sustain.* **7**, 158–167 (2024).
18. H. Jin, J. Xu, H. Liu, H. Shen, H. Yu, M. Jaroniec, Y. Zheng, S.-Z. Qiao, Emerging materials and technologies for electrocatalytic seawater splitting. *Sci. Adv.* **9**, eadi7755 (2023).
19. J. Guo, Y. Zheng, Z. Hu, C. Zheng, J. Mao, K. Du, M. Jaroniec, S.-Z. Qiao, T. Ling, Direct seawater electrolysis by adjusting the local reaction environment of a catalyst. *Nat. Energy* **8**, 264–272 (2023).
20. X. Duan, Q. Sha, P. Li, T. Li, G. Yang, W. Liu, E. Yu, D. Zhou, J. Fang, W. Chen, Y. Chen, L. Zheng, J. Liao, Z. Wang, Y. Li, H. Yang, G. Zhang, Z. Zhuang, S. F. Hung, C. Jing, J. Luo, L. Bai, J. Dong, H. Xiao, W. Liu, Y. Kuang, B. Liu, X. Sun, Dynamic chloride ion adsorption on single iridium atom boosts seawater oxidation catalysis. *Nat. Commun.* **15**, 1973 (2024).
21. M. M. Najafpour, G. Renger, M. Hołynska, A. N. Moghaddam, E.-M. Aro, R. Carpentier, H. Nishihara, J. J. Eaton-Rye, J.-R. Shen, S. I. Allakhverdiev, Manganese compounds as water-oxidizing catalysts: From the natural water-oxidizing complex to nanosized manganese oxide structures. *Chem. Rev.* **116**, 2886–2936 (2016).
22. Z. Mei, G. Zhao, C. Xia, S. Cai, Q. Jing, X. Sheng, H. Wang, X. Zou, L. Wang, H. Guo, B. Xia, Regulated high-spin state and constrained charge behavior of active cobalt sites in covalent organic frameworks for promoting electrocatalytic oxygen reduction. *Angew. Chem. Int. Ed. Engl.* **62**, e202303871 (2023).
23. Y. Liu, Y. Chen, Y. Tian, T. Sakthivel, H. Liu, S. Guo, H. Zeng, Z. Dai, Synergizing hydrogen spillover and deprotonation by the internal polarization field in a MoS_2/$NiPS_3$ vertical heterostructure for boosted water electrolysis. *Adv. Mater.* **34**, e2203615 (2022).
24. F. Yang, M. Lopez Luna, F. T. Haase, D. Escalera-López, A. Yoon, M. Rüscher, C. Rettenmaier, H. S. Jeon, E. Ortega, J. Timoshenko, A. Bergmann, S. W. Chee, B. R. Cuenya, Spatially and chemically resolved visualization of Fe incorporation into NiO octahedra during the oxygen evolution reaction. *J. Am. Chem. Soc.* **145**, 21465–21474 (2023).
25. C.-Y. Huang, H.-M. Lin, C.-H. Chiang, H.-A. Chen, T.-R. Liu, S. K. Deepak Vishnu, J.-W. Chiou, R. Sankar, H.-M. Tsai, W.-F. Pong, C.-W. Chen, Manipulating spin exchange interactions and spin-selected electron transfers of 2D metal phosphorus trisulfide crystals for efficient oxygen evolution reaction. *Adv. Funct. Mater.* **33**, 2305792 (2023).
26. D. Liu, M. Lu, D. Liu, S. Yan, W. Zhou, L. Zhang, Z. Zou, Heat-triggered ferri-to-paramagnetic transition accelerates redox couple-mediated electrocatalytic water oxidation. *Adv. Funct. Mater.* **32**, 2111234 (2022).
27. F. Dong, H. Duan, Z. Lin, H. Yuan, M. Ju, X. Du, J. Gao, J. Yu, S. Yang, Unravelling the effect of Cl-on alkaline saline water electrooxidation on NiFe (oxy)hydroxides. *Appl. Catal. B.* **340**, 123242 (2024).
28. Y. Liu, L. Li, L. Wang, N. Li, X. Zhao, Y. Chen, T. Sakthivel, Z. Dai, Janus electronic state of supported iridium nanoclusters for sustainable alkaline water electrolysis. *Nat. Commun.* **15**, 2851 (2024).
29. Q. Fu, L. W. Wong, F. Zheng, X. Zheng, C. S. Tsang, K. H. Lai, W. Shen, T. H. Ly, Q. Deng, J. Zhao, Unraveling and leveraging in situ surface amorphization for enhanced hydrogen evolution reaction in alkaline media. *Nat. Commun.* **14**, 6462 (2023).
30. Z. Guo, H. Zhang, S. Lu, Z. Wang, S. Tang, J. Shao, Z. Sun, H. Xie, H. Wang, X. F. Yu, P. K. Chu, From black phosphorus to phosphorene: Basic solvent exfoliation, evolution of Raman scattering, and applications to ultrafast photonics. *Adv. Funct. Mater.* **25**, 6996–7002 (2015).
31. J. Song, S. Qiu, F. Hu, Y. Ding, S. Han, L. Li, H. Y. Chen, X. Han, C. Sun, S. Peng, Sub-2 nm thiophosphate nanosheets with heteroatom doping for enhanced oxygen electrocatalysis. *Adv. Funct. Mater.* **31**, 2100618 (2021).
32. X. Li, Z. Wang, B. Zhang, A. I. Rykov, M. A. Ahmed, J. Wang, $Fe_xCo_{3-x}O_4$ nanocages derived from nanoscale metal-organic frameworks for removal of bisphenol A by activation of peroxymonosulfate. *Appl. Catal. B* **181**, 788–799 (2016).
33. H. Yang, L. Gong, H. Wang, C. Dong, J. Wang, K. Qi, H. Liu, X. Guo, B. Y. Xia, Preparation of nickel-iron hydroxides by microorganism corrosion for efficient oxygen evolution. *Nat. Commun.* **11**, 5075 (2020).
34. S. Xu, S. Feng, Y. Yu, D. Xue, M. Liu, C. Wang, K. Zhao, B. Xu, J.-N. Zhang, Dual-site segmentally synergistic catalysis mechanism: Boosting $CoFeS_x$ nanocluster for sustainable water oxidation. *Nat. Commun.* **15**, 1720 (2024).
35. Q. Niu, M. Yang, D. Luan, N. Li, L. Yu, X. W. Lou, Construction of Ni-Co-Fe hydr(oxy)oxide@ Ni-Co layered double hydroxide yolk-shelled microrods for enhanced oxygen evolution. *Angew. Chem. Int. Ed. Engl.* **61**, e202213049 (2022).
36. D. Voiry, M. Chhowalla, Y. Gogotsi, N. A. Kotov, Y. Li, R. M. Penner, R. E. Schaak, P. S. Weiss, Best practices for reporting electrocatalytic performance of nanomaterials. *ACS Nano* **12**, 9635–9638 (2018).
37. Y. Liu, P. Vijayakumar, Q. Liu, T. Sakthivel, F. Chen, Z. Dai, Shining light on anion-mixed nanocatalysts for efficient water electrolysis: Fundamentals, progress, and perspectives. *Nano-Micro Lett.* **14**, 43 (2022).
38. M. W. Louie, A. T. Bell, An investigation of thin-film Ni-Fe oxide catalysts for the electrochemical evolution of oxygen. *J. Am. Chem. Soc.* **135**, 12329–12337 (2013).
39. H. Sun, L. Chen, Y. Lian, W. Yang, L. Lin, Y. Chen, J. Xu, D. Wang, X. Yang, M. H. Rümmerli, J. Guo, J. Zhong, Z. Deng, Y. Jiao, Y. Peng, S. Qiao, Topotactically transformed polygonal mesopores on ternary layered double hydroxides exposing under-coordinated metal centers for accelerated water dissociation. *Adv. Mater.* **32**, e2006784 (2020).
40. W. Tang, G. Zhang, Y. Qiu, FeOOH/Ni heterojunction nanoarrays on carbon cloth as a robust catalyst for efficient oxygen evolution reaction. *Int. J. Hydrogen Energy* **45**, 28566–28575 (2020).
41. J. Zhang, J. Liu, L. Xi, Y. Yu, N. Chen, S. Sun, W. Wang, K. M. Lange, B. Zhang, Single-atom Au/NiFe layered double hydroxide electrocatalyst: Probing the origin of activity for oxygen evolution reaction. *J. Am. Chem. Soc.* **140**, 3876–3879 (2018).
42. X. Bo, R. K. Hocking, S. Zhou, Y. Li, X. Chen, J. Zhuang, Y. Du, C. Zhao, Capturing the active sites of multimetallic (oxy)hydroxides for the oxygen evolution reaction. *Energ. Environ. Sci.* **13**, 4225–4237 (2020).
43. Q. Lv, Z. Zhu, Y. Ni, J. Geng, F. Li, Spin-state manipulation of two-dimensional metal-organic framework with enhanced metal-oxygen covalency for lithium-oxygen batteries. *Angew. Chem. Int. Ed. Engl.* **61**, e202114293 (2022).
44. R. R. Chen, Y. Sun, S. J. H. Ong, S. Xi, Y. Du, C. Liu, O. Lev, Z. J. Xu, Antiferromagnetic inverse spinel oxide $LiCoVO_4$ with spin-polarized channels for water oxidation. *Adv. Mater.* **32**, e1907976 (2020).
45. Y. Fang, K. Zhuang, H. Cui, Z. Zhang, A. Wang, C. Wang, D. Zheng, X. Wang, The state of Fe^{3+} in the C-F-A-S-H system with varying Fe/Si and Ca/Si ratios. *J. Mater. Chem. A* **11**, 26193–26211 (2023).
46. G. Yang, J. Zhu, P. Yuan, Y. Hu, G. Qu, B.-A. Lu, X. Xue, H. Yin, W. Cheng, J. Cheng, W. Xu, J. Li, J. Hu, S. Mu, J. N. Zhang, Regulating Fe-spin state by atomically dispersed Mn-N in Fe-NC catalysts with high oxygen reduction activity. *Nat. Commun.* **12**, 1734 (2021).
47. D. Xia, X. Tang, S. Dai, R. Ge, A. Rykov, J. Wang, T. H. Huang, K. W. Wang, Y. Wei, K. Zhang, J. Li, L. Gan, F. Kang, Ultrastable Fe-N-C fuel cell electrocatalysts by eliminating non-coordinating nitrogen and regulating coordination structures at high temperatures. *Adv. Mater.* **35**, e2204474 (2023).
48. Y. Ma, Y. Hu, Y. Pramudya, T. Diemant, Q. Wang, D. Goonetilleke, Y. Tang, B. Zhou, H. Hahn, W. Wenzel, M. Fichtner, Y. Ma, B. Breitung, T. Brezesinski, Resolving the role of configurational entropy in improving cycling performance of multicomponent hexacyanoferrate cathodes for sodium-ion batteries. *Adv. Funct. Mater.* **32**, 2202372 (2022).
49. H. Li, P. Shi, L. Wang, T. Yan, T. Guo, X. Xia, C. Chen, J. Mao, D. Sun, L. Zhang, Cooperative catalysis of polysulfides in lithium-sulfur batteries through adsorption competition by tuning cationic geometric configuration of dual-active sites in spinel oxides. *Angew. Chem. Int. Ed. Engl.* **62**, e202216286 (2023).
50. D. Wang, Y. Jiao, W. Shi, B. Pu, F. Ning, J. Yi, Y. Ren, J. Yu, Y. Li, H. Wang, B. Li, Y. Li, C. Nan, L. Chen, S. Shi, Fundamentals and advances of ligand field theory in understanding structure-electrochemical property relationship of intercalation-type electrode materials for rechargeable batteries. *Prog. Mater. Sci.* **133**, 101055 (2023).
51. J. Wei, Y. Shao, J. Xu, F. Yin, Z. Li, H. Qian, Y. Wei, L. Chang, Y. Han, J. Li, L. Gan, Sequential oxygen evolution and decoupled water splitting via electrochemical redox reaction of nickel hydroxides. *Nat. Commun.* **15**, 9012 (2024).
52. K. Mathew, R. Sundararaman, K. Letchworth-Weaver, T. Arias, R. G. Hennig, Implicit solvation model for density-functional study of nanocrystal surfaces and reaction pathways. *J. Chem. Phys.* **140**, 084106 (2014).
53. K. Mathew, V. Kolluru, S. Mula, S. N. Steinmann, R. G. Hennig, Implicit self-consistent electrolyte model in plane-wave density-functional theory. *J. Chem. Phys.* **151**, 234101 (2019).
54. H. Liu, W. Shen, H. Jin, J. Xu, P. Xi, J. Dong, Y. Zheng, S. Z. Qiao, High-performance alkaline seawater electrolysis with anomalous chloride promoted oxygen evolution reaction. *Angew. Chem. Int. Ed. Engl.* **62**, e202311674 (2023).
55. R. Dangol, Z. Dai, A. Chaturvedi, Y. Zheng, Y. Zhang, K. N. Dinh, B. Li, Y. Zong, Q. Yan, Few-layer $NiPS_3$ nanosheets as bifunctional materials for Li-ion storage and oxygen evolution reaction. *Nanoscale* **10**, 4890–4896 (2018).
56. B. Ravel, M. Newville, ATHENA, ARTEMIS, HEPHAESTUS: Data analysis for X-ray absorption spectroscopy using IFEFFIT. *J. Synchrotron Radiat.* **12**, 537–541 (2005).
57. G. Kresse, J. Furthmüller, Efficient iterative schemes for ab initio total-energy calculations using a plane-wave basis set. *Phys. Rev. B* **54**, 11169–11186 (1996).
58. J. P. Perdew, K. Burke, M. Ernzerhof, Generalized gradient approximation made simple. *Phys. Rev. Lett.* **77**, 3865–3868 (1996).

59. S. Grimme, J. Antony, S. Ehrlich, H. Krieg, A consistent and accurate ab initio parametrization of density functional dispersion correction (DFT-D) for the 94 elements H-Pu. *J. Chem. Phys.* **132**, 154104 (2010).
60. T. X. Nguyen, J. Patra, C. C. Tsai, W. Y. Xuan, H. Y. T. Chen, M. S. Dyer, O. Clemens, J. Li, S. B. Majumder, J. K. Chang, J. M. Ting, Secondary-phase-induced charge-discharge performance enhancement of Co-free high entropy spinel oxide electrodes for Li-ion batteries. *Adv. Funct. Mater.* **33**, 2300509 (2023).
61. B. Zhang, L. Wang, Z. Cao, S. M. Kozlov, F. P. García de Arquer, C. T. Dinh, J. Li, Z. Wang, X. Zheng, L. Zhang, Y. Wen, O. Voznyy, R. Comin, P. de Luna, T. Regier, W. Bi, E. E. Alp, C. W. Pao, L. Zheng, Y. Hu, Y. Ji, Y. Li, Y. Zhang, L. Cavallo, H. Peng, E. H. Sargent, High-valence metals improve oxygen evolution reaction performance by modulating 3d metal oxidation cycle energetics. *Nat. Catal.* **3**, 985–992 (2020).
62. H. J. Monkhorst, J. D. Pack, Special points for Brillouin-zone integrations. *Phys. Rev. B* **13**, 5188–5192 (1976).
63. Y. J. Lee, S. K. Park, Metal-organic framework-derived hollow CoS_x nanoarray coupled with NiFe layered double hydroxides as efficient bifunctional electrocatalyst for overall water splitting. *Small* **18**, e2200586 (2022).
64. Y. Gong, Z. Yang, Y. Lin, J. Wang, H. Pan, Z. Xu, Hierarchical heterostructure $NiCo_2O_4$@ $CoMoO_4$/NF as an efficient bifunctional electrocatalyst for overall water splitting. *J. Mater. Chem. A* **6**, 16950–16958 (2018).
65. J. Wang, J. Hu, S. Niu, S. Li, Y. Du, P. Xu, Crystalline-amorphous $Ni_2P_4O_{12}$/$NiMoO_x$ nanoarrays for alkaline water electrolysis: Enhanced catalytic activity via in situ surface reconstruction. *Small* **18**, e2105972 (2022).
66. L. Guo, Q. Liu, Y. Liu, Z. Chen, Y. Jiang, H. Jin, T. Zhou, J. Yang, Y. Liu, Self-supported tremella-like MoS_2-AB particles on nickel foam as bifunctional electrocatalysts for overall water splitting. *Nano Energy* **92**, 106707 (2022).
67. C. Ray, S. C. Lee, K. V. Sankar, B. Jin, J. Lee, J. H. Park, S. C. Jun, Amorphous phosphorus-incorporated cobalt molybdenum sulfide on carbon cloth: An efficient and stable electrocatalyst for enhanced overall water splitting over entire pH values. *ACS Appl. Mater. Interfaces* **9**, 37739–37749 (2017).
68. W. Xu, S. Zhu, Y. Liang, Z. Cui, X. Yang, A. Inoue, A nanoporous metal phosphide catalyst for bifunctional water splitting. *J. Mater. Chem. A* **6**, 5574–5579 (2018).
69. G. Song, S. Luo, Q. Zhou, J. Zou, Y. Lin, L. Wang, G. Li, A. Meng, Z. Li, Doping and heterojunction strategies for constructing V-doped Ni_3FeN/Ni anchored on N-doped graphene tubes as an efficient overall water splitting electrocatalyst. *J. Mater. Chem. A* **10**, 18877–18888 (2022).
70. W. Tang, X. Liu, Y. Li, Y. Pu, Y. Lu, Z. Song, Q. Wang, R. Yu, J. Shui, Boosting electrocatalytic water splitting via metal-metalloid combined modulation in quaternary Ni-Fe-PB amorphous compound. *Nano Res.* **13**, 447–454 (2020).
71. X. Zhao, P. Pachfule, S. Li, J. R. J. Simke, J. Schmidt, A. Thomas, Bifunctional electrocatalysts for overall water splitting from an iron/nickel-based bimetallic metal-organic framework/dicyandiamide composite. *Angew. Chem. Int. Ed. Engl.* **57**, 8921–8926 (2018).
72. D. Kim, Y. Jeong, H. Roh, C. Lim, K. Yong, Biomimetic 2D-Ni(Co, Fe)P/1D-WO_x nanocoral reef electrocatalysts for efficient water splitting. *J. Mater. Chem. A* **9**, 10909–10920 (2021).
73. M. Wang, L. Zhang, J. Pan, M. Huang, H. Zhu, A highly efficient Fe-doped Ni_3S_2 electrocatalyst for overall water splitting. *Nano Res.* **14**, 4740–4747 (2021).
74. J. Ma, X. Lu, C. Wang, S. Wang, W. He, B. Zhang, L. Shao, X. Zhai, J. Han, S. Feng, Y. Fu, W. Qi, Synthesis of amorphous FeNiCo trimetallic hybrid electrode from ZIF precursors for efficient oxygen evolution reaction. *Nanotechnology* **33**, 035403 (2022).
75. H. Liu, X. Xu, H. Xu, S. Wang, Z. Niu, Q. Jia, L. Yang, R. Cao, L. Zheng, D. Cao, Dual active site tandem catalysis of metal hydroxyl oxides and single atoms for boosting oxygen evolution reaction. *Appl. Catal. B* **297**, 120451 (2021).
76. Y. Liu, S. Jiang, S. Li, L. Zhou, Z. Li, J. Li, M. Shao, Interface engineering of (Ni, Fe)S_2@MoS_2 heterostructures for synergetic electrochemical water splitting. *Appl. Catal. B* **247**, 107–114 (2019).
77. Q. Wen, K. Yang, D. Huang, G. Cheng, X. Ai, Y. Liu, J. Fang, H. Li, L. Yu, T. Zhai, Schottky heterojunction nanosheet array achieving high-current-density oxygen evolution for industrial water splitting electrolyzers. *Adv. Energy Mater.* **11**, 2102353 (2021).
78. H. Liu, Z. Liu, F. Wang, L. Feng, Efficient catalysis of N doped NiS/NiS_2 heterogeneous structure. *Chem. Eng. J.* **397**, 125507 (2020).
79. Q. Li, D. Wang, C. Han, X. Ma, Q. Lu, Z. Xing, X. Yang, Construction of amorphous interface in an interwoven NiS/NiS_2 structure for enhanced overall water splitting. *J. Mater. Chem. A* **6**, 8233–8237 (2018).
80. J. Nai, X. Xu, Q. Xie, G. Lu, Y. Wang, D. Luan, X. Tao, X. W. Lou, Construction of $Ni(CN)_2$/$NiSe_2$ heterostructures by stepwise topochemical pathways for efficient electrocatalytic oxygen evolution. *Adv. Mater.* **34**, e2104405 (2022).
81. F. Luo, Q. Zhang, X. Yu, S. Xiao, Y. Ling, H. Hu, L. Guo, Z. Yang, L. Huang, W. Cai, H. Cheng, Palladium phosphide as a stable and efficient electrocatalyst for overall water splitting. *Angew. Chem. Int. Ed. Engl.* **57**, 14862–14867 (2018).
82. T. Zheng, C. Shang, Z. He, X. Wang, C. Cao, H. Li, R. Si, B. Pan, S. Zhou, J. Zeng, Intercalated iridium diselenide electrocatalysts for efficient pH-universal water splitting. *Angew. Chem. Int. Ed. Engl.* **58**, 14764–14769 (2019).
83. T. Zhu, J. Huang, B. Huang, N. Zhang, S. Liu, Q. Yao, S. C. Haw, Y. C. Chang, C. W. Pao, J. M. Chen, Q. Shao, Z. Hu, Y. Ma, X. Huang, High-index faceted RuCo nanoscrews for water electrosplitting. *Adv. Energy Mater.* **10**, 2002860 (2020).
84. M. Chen, D. Liu, B. Zi, Y. Chen, D. Liu, X. Du, F. Li, P. Zhou, Y. Ke, J. Li, Remarkable synergistic effect in cobalt-iron nitride/alloy nanosheets for robust electrochemical water splitting. *J. Energy Chem.* **65**, 405–414 (2022).
85. S. Sun, C. Lv, W. Hong, X. Zhou, F. Wu, G. Chen, Dual tuning of composition and nanostructure of hierarchical hollow nanopolyhedra assembled by NiCo-layered double hydroxide nanosheets for efficient electrocatalytic oxygen evolution. *ACS Appl. Energy Mater.* **2**, 312–319 (2018).
86. Y. Li, T. Zhao, M. Lu, Y. Wu, Y. Xie, H. Xu, J. Gao, J. Yao, G. Qian, Q. Zhang, Enhancing oxygen evolution reaction through modulating electronic structure of trimetallic electrocatalysts derived from metal-organic frameworks. *Small* **15**, e1901940 (2019).
87. C. Han, L. Zhong, Q. Sun, D. Chen, T.-T. Li, Y. Hu, J. Qian, S. Huang, Electrochemical evolution of cobalt-carboxylate framework for efficient water oxidation. *J. Power Sources* **499**, 229947 (2021).
88. D. Yang, W. Hou, Y. Lu, W. Zhang, Y. Chen, Cobalt phosphide nanoparticles supported within network of N-doped carbon nanotubes as a multifunctional and scalable electrocatalyst for water splitting. *J. Energy Chem.* **52**, 130–138 (2021).

Acknowledgments: We thank M. Liu at Instrument Analysis Center of Xi'an Jiaotong University for the assistance with XPS analysis. We thank the Anhui Absorption Spectroscopy Analysis Instrument Co. Ltd. for XAFS measurements and analysis. This research used the resources of the HPCC platform in Xi'an Jiaotong University. XAFS experiment measurements were performed at SPring-8 under proposal numbers 2024A1566 and 2023A1735 for XAFS. **Funding:** This work was supported by the National Natural Science Foundation of China grant 52371236 (Z.D.), Shaanxi Province Key Research and Development Plan grant 2024GX-ZDCYL-01-06 (Z.D.), Science Fund for Distinguished Young Scholars of Shaanxi Province grant 2024JC-JCQN-09 (Z.G.), AcRF Tier 2 grant MOE-T2EP10123-0003 from MOE-Singapore (D.W.), and National Key R&D Program of China grant 2024YFE0109200 (X.Z.). **Author contributions:** Conceptualization: Y.L., X.Z., and Z.D. Methodology: Y.L. and X.Z. Investigation: Y.L., L.L., X.L., Y.X., D.W., T.S., X.Z., and Z.D. Visualization: Y.L., X.Z., and Z.D. Data curation: Y.L., X.L., Y.X., Z.G., and X.Z. Formal analysis: Y.L., Z.G., and X.Z. Funding acquisition: D.W. and Z.D. Resources: L.L., X.L., Y.X., X.Z., and Z.D. Software: L.L. Project administration: Z.D. Supervision: Z.D. Validation: Y.L., X.L., Y.X., D.W., and X.Z. Writing—original draft: Y.L., X.Z., and Z.D. Writing—review and editing: Y.L., X.L., Y.X., D.W., Z.G., X.Z., and Z.D. **Competing interests:** The authors declare that they have no competing interests. **Data and materials availability:** All data needed to evaluate the conclusions in the paper are present in the paper and/or the Supplementary Materials.

Submitted 30 July 2024
Accepted 25 April 2025
Published 30 May 2025
10.1126/sciadv.ads0861